Development of a Rayleigh Scattering Diagnostic for Time-Resolved Gas Flow Velocity, Temperature, and Density Measurements in Aerodynamic Test Facilities

A. F. Mielke*, K. A. Elam†, C. J. Sung‡

*NASA Glenn Research Center, 21000 Brookpark Road, M.S. 77-1, Cleveland, OH 44135
†Jacobs Sverdrup, Cleveland, OH 44135
‡Case Western Reserve University, Cleveland, OH 44106

***Abstract*- A molecular Rayleigh scattering technique is developed to measure time-resolved gas velocity, temperature, and density in unseeded turbulent flows at sampling rates up to 32 kHz. A high power continuous-wave laser beam is focused at a point in an air flow field and Rayleigh scattered light is collected and fiber-optically transmitted to the spectral analysis and detection equipment. The spectrum of the light, which contains information about the temperature and velocity of the flow, is analyzed using a Fabry-Perot interferometer. Photomultipler tubes operated in the photon counting mode allow high frequency sampling of the circular interference pattern to provide time-resolved flow property measurements. An acoustically driven nozzle flow is studied to validate velocity fluctuation measurements, and an asymmetric oscillating counterflow with unequal enthalpies is studied to validate the measurement of temperature fluctuations. Velocity fluctuations are compared with constant temperature anemometry measurements and temperature fluctuations are compared with constant current anemometry measurements at the same locations. Time-series and power spectra of the temperature and velocity measurements are presented. A numerical simulation of the light scattering and detection process was developed and compared with experimental data for future use as an experiment design tool.**

NOMENCLATURE

$A(i)$	amplitude of sine wave at i^{th} harmonic frequency
a	most probable molecular speed (m s^{-1})
c	speed of light (= 2.998 x 10^8 m s^{-1})
d	Fabry-Perot mirror spacing (m)
$\mathbf{E}$	incident electric field vector (V m^{-1})
F	Fabry-Perot instrument function contrast
f	frequency of scattered light (s^{-1})
f_0	frequency of incident laser light (s^{-1})
f_{fund}	fundamental frequency (Hz)
f_C	collimating lens focal length (m)
f_L	fringe forming lens focal length (m)
f_s	sampling rate (s^{-1})
h	Planck's constant (= 6.626 x 10^{-34} N m s)
I_{FP}	Fabry-Perot instrument function
$\mathbf{K}$	interaction wave vector (m^{-1})
K	magnitude of $\mathbf{K}$ (m^{-1})
$\mathbf{k_0}$	incident light wave vector (m^{-1})
$\mathbf{k_s}$	scattered light wave vector (m^{-1})
L	length of sub-records in spectral calculations
L_x	probe volume length (m)
l_m	mean free path between molecular collisions (m)
m	molecular mass (kg)
N_e	effective finesse
N_q	photoelectron counts at q^{th} annular region
N_R	Rayleigh scattered photoelectrons collected into solid angle Ω
n	molecular number density (m^{-3})
P_0	power of incident laser beam (J s^{-1})
p	static pressure (N m^{-2})
q	annular region number
r	radial position in image plane (m)
r_j	radial position in the jet measurement plane (m)
r_{max}	fiber face image radius (m)
r_q	inner radius of q^{th} annular region (m)
r_R	fringe radius for reference laser light (m)
S_R	Rayleigh scattering spectrum
T	static temperature (K)
$\mathbf{u}$	velocity vector (m s^{-1})
u_k	measured velocity component (m s^{-1})
x_f	non-dimensionalized frequency
y	y-parameter
β	angle between $\mathbf{E}$ and scattering plane (rad)
Γ	Fisher information matrix
Δr	width of annular region (m)
Δt	integration time (s)
ε	optical system efficiency
η	dynamic viscosity (N s m^{-2})
θ	angle between light ray and optical axis (rad)
θ_R	angle between reference ray and optical axis (rad)
κ	Boltzmann's constant (= 1.381 x 10^{-23} J K^{-1})
Λ	wavelength corresponding to wave vector $\mathbf{K}$ (m)
λ	illumination wavelength (m)
μ	refractive index
ρ	gas density (kg m^{-3})
$\frac{d\sigma}{d\Omega}$	differential scattering cross-section (m^2 sr^{-1})
χ_s	scattering angle (rad)
ψ	phase change between successive reflections
Ω	solid angle (sr)

I. Introduction

There is currently no high frequency response, non-intrusive temperature measurement technique for use in turbulent flow studies. There are also no techniques that can provide non-intrusive time-resolved measurement of gas temperature, velocity, and density simultaneously. Conventional intrusive measurement devices such as resistance wires, pressure probes, and thermocouples are usually limited in spatial and temporal resolution, disturb the flow under study, and can be damaged by high pressure or temperature. Therefore, a non-intrusive molecular Rayleigh scattering technique is developed to measure time-resolved gas temperature, velocity, and density in unseeded turbulent flows at sampling rates up to 32 kHz.

Various optical techniques are available for temperature, molecular number density, and velocity measurements. Eckbreth provides the details of several techniques, such as Coherent Anti-Stokes Raman Spectroscopy (CARS), Spontaneous Raman and Rayleigh scattering, and Laser-Induced Fluorescence (LIF), with an emphasis on their use in combustion applications [1]. Other techniques that have been used for flow measurements in various environments include Laser-Induced Thermal Acoustics (LITA) [2,3], also known as Transient Grating Spectroscopy (TGS) [4], Laser-Doppler Velocimetry (LDV) [5-8], filtered Rayleigh scattering [9], Particle Image Velocimetry (PIV) [10], and focusing schlieren deflectometry [11]. However, none of these techniques can provide high frequency response measurement of all three flow properties simultaneously.

The temporal response of most of the optical measurement techniques mentioned here is typically limited by the repetition rate of pulsed lasers; usually on the order of 10-100 Hz. One can potentially take many snap shots to obtain rms turbulence measurements, however this type of measurement does not provide power spectral content. Recent advances in laser and camera technology has led to the development of temporally resolved PIV, which provides planar velocity measurements at rates up to 25 kHz [10]. Signal strength of the scattering process can also limit the temporal response. Rayleigh scattering has several advantages over other light scattering techniques; the Rayleigh scattering cross-section is three orders of magnitude greater than the Raman scattering cross-section, and Rayleigh scattering is generally much simpler and lower cost to implement than techniques that require multiple lasers and have other complicating factors.

Previous works using molecular Rayleigh scattering to make temperature, velocity, and number density measurements in harsh environments [12-15], and dynamic density and velocity measurements in supersonic free jets [16,17] have been reported. The current work describes further development and validation of a technique previously reported in [18] and [19] in which dynamic temperature, velocity, and density measurements were made in a low speed heated jet and an acoustically driven flow up to 16 kHz.

The Rayleigh scattering technique presented is unique in that it provides simultaneous temperature, velocity, and density fluctuation measurements. A high power continuous-wave (cw) laser beam is focused at a point in an air flow field and Rayleigh scattered light is collected and transmitted via optical fiber to another location where the light is spectrally resolved. The spectrum of the light contains information about the temperature, velocity, and density of the flow. A planar mirror Fabry-Perot interferometer (FPI) is used to analyze the spectrum of the scattered light, and photomultiplier tubes (PMTs) record the fringe intensity pattern at high sampling rates enabling time-resolved measurement of the gas flow properties. Further development of the technique since the previously reported work [19] includes increasing the maximum sampling rate and performing improved validation studies. An acoustically modulated nozzle flow was used to validate the velocity fluctuation and frequency measurements, and an asymmetric oscillating counterflow with unequal enthalpies was used to verify the temperature fluctuation and frequency measurements by comparison with hotwire and coldwire probe measurements.

The ability to obtain high frequency response measurements of multiple properties simultaneously is a valuable tool for compressible, turbulent flow research. These data are particularly useful to aeroacoustics researchers who are interested in correlating flow property fluctuations with far field acoustic fluctuations. Knowledge of velocity-temperature fluctuation correlations is also needed to improve computational fluid dynamic (CFD) models of compressible turbulent flows. The ability to route the signal, and potentially the incident illumination, via fiber optics makes this technique appealing to facilities researchers who typically require flow measurements in harsh environments with tight space constraints.

In response to NASA's mission to reduce aircraft noise levels, the contribution of temperature fluctuations to far-field noise will be evaluated experimentally by application of the presented Rayleigh scattering technique in the Supersonic Hot Jet Acoustic Rig (SHJAR), which is a heated nozzle facility located in the AeroAcoustic Propulsion Laboratory (AAPL) at NASA Glenn Reaseach Center (GRC). Sound pressure fluctuation (microphone) measurements will be acquired simultaneously with Rayleigh measurements allowing correlation between flow property fluctuations and noise generation. Determining sources of jet noise will help engineers to design quieter, more efficient aircraft.

II. Theoretical Study

A. Rayleigh scattering and spectral analysis

Molecular Rayleigh scattering is the result of elastic light scattering from gas molecules. When light from a single frequency laser beam passes through a gas, the scattered light is shifted in frequency by the Doppler effect due to the thermal as well as the bulk motion of the molecules. The frequency spectrum of the scattered light contains information about the gas density, bulk velocity, and temperature. Fig. 1 shows a

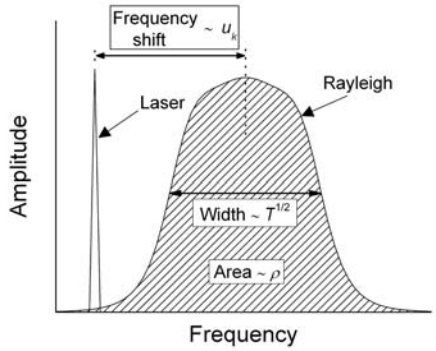

Figure 1. Rayleigh scattering spectrum.

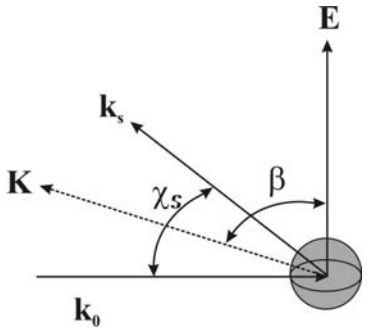

Figure 2. Light scattering from a moving particle.

Rayleigh scattering spectrum containing the narrow laser line and a typical Rayleigh spectral peak to illustrate how the flow property measurements are obtained from the spectral information. If the gas composition is fixed, the total intensity of the Rayleigh scattered light is directly proportional to the gas density. The frequency shift between the laser peak and the Rayleigh peak is proportional to the bulk flow velocity. The width of the spectrum is related to the gas temperature.

The shape of the spectrum is dependent on gas pressure, temperature and the scattering angle [20]. A non-dimensional parameter y, which represents the ratio of the wavelength of the scattering grating $\left(\Lambda = \frac{\lambda}{2\sin\frac{\chi_s}{2}} \right)$ to the mean free path between molecular collisions $\left(l_m = \frac{a\eta}{n\kappa T} \right)$, is used to establish spectral shape regimes:

$$y = \frac{\Lambda}{2\pi\, l_m} = \frac{p}{\eta K a} \tag{1}$$

where $a = \sqrt{\frac{2\kappa T}{m}}$ (2)

The interaction wave vector, which defines the direction of the velocity component being measured, is the bisector of the incident and scattered light wave vectors (Fig. 2). The interaction wave vector and its magnitude are given by:

$$\mathbf{K} = \mathbf{k_s} - \mathbf{k_0} \tag{3}$$

$$K = |\mathbf{K}| = \frac{4\pi}{\lambda}\left[\sin\frac{\chi_s}{2}\right] \tag{4}$$

The geometry of the optical arrangement in an experiment can be designed such that the desired component of the velocity is measured:

$$u_k = \frac{\mathbf{K}\cdot\mathbf{u}}{K} \tag{5}$$

Three spectral shape regimes are defined for typical 90° scattering [20-22]. The shape regimes are illustrated in Fig. 3, where the normalized frequency is defined as:

$$x_f = \frac{2\pi(f - f_0)}{Ka} \tag{6}$$

For low density gases where $y << 1$, the Rayleigh spectrum is accurately modeled by a Gaussian function and the gas is said to be in the Knudsen or collisionless regime. For higher density gases where $y >> 1$, the Rayleigh spectrum broadens and eventually develops side-lobes known as Brillouin peaks. This is known as the hydrodynamic or continuum regime where molecular collisions are the dominant process. Finally, for $0.2 \le y \le 2$, as is the case in the present experiments, the gas is in a transition region between the collisionless and hydrodynamic regimes, and a kinetic theory model is required.

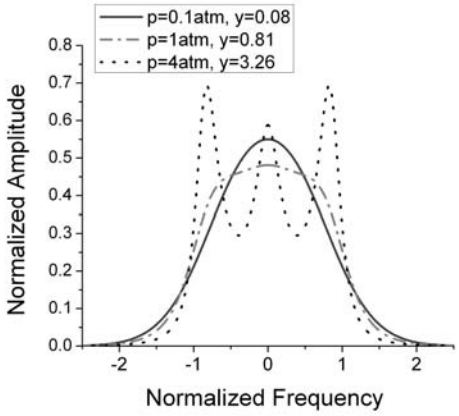

Figure 3. Rayleigh scattering spectrum for various y-parameters.

A kinetic theory model developed by G. Tenti (TENTI S6) provides a description of Rayleigh-Brillouin scattering from molecular gases in all density regimes [20,23]. This spectrum model was used to generate the information displayed in Figs. 1 and 3, and is incorporated in the model function used in least squares analysis of the experimental data.

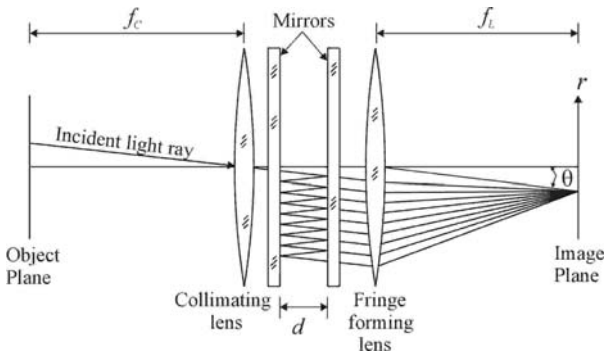

Figure 4. Fabry-Perot interferometer.

The spectrum of the Rayleigh scattered light is analyzed using a planar mirror FPI (Fig. 4) operated in the static imaging mode [24]. The fringe intensity pattern is a function of both the Rayleigh spectrum and the Fabry-Perot instrument function. The Fabry-Perot instrument function is:

$$I_{FP}(x_f, r) = \frac{1}{1 + F \sin^2 \dfrac{\psi(x_f, r)}{2}} \tag{7}$$

where $$F = \frac{1}{\sin^2\left(\dfrac{\pi}{2N_e}\right)} \tag{8}$$

$$\psi = \frac{4\pi\mu d}{\lambda}\left[\frac{\theta_R^2 - \theta^2}{2} + \frac{\lambda a}{c\Lambda} x_f\right] \tag{9}$$

$$\theta = r/f_L \tag{10}$$

In our experiment, Rayleigh scattered light from a defined probe volume is collected into a multimode optical fiber. The light exiting the fiber is collimated and directed to the FPI, and a lens at the interferometer output focuses the interference fringe pattern at the image plane. The total expected number of Rayleigh photoelectron counts *without* the FPI in the optical path can be expressed as:

$$\langle N_R \rangle = \frac{\varepsilon P_0 n L_x \lambda \Omega \Delta t}{h c}\left(\frac{d\sigma}{d\Omega}\right)\sin^2\beta \tag{11}$$

where the overall system efficiency ε includes detector quantum efficiency and other losses. When the interferometer is placed in the light path, the amount of energy collected from the q^{th} annular region of the interference pattern, which has been dissected into one circular and three annular regions, in terms of photoelectron counts, can be expressed by the following model function:

$$\langle N_q \rangle = \frac{\langle N_R \rangle}{\pi r_{\max}^2} \int_{r_q}^{r_q + \Delta r} \int_{-\infty}^{\infty} S_R(x_f)\, I_{FP}(x_f, r)\, dx_f\, dr \tag{12}$$

where the Rayleigh spectrum S_R is evaluated using the TENTI S6 model.

B. Lower bound for measurement uncertainty

The lower bound on the uncertainty in temperature, velocity, and density measurements using Rayleigh scattering is set by the photon statistical (shot) noise. Estimates of the measurement uncertainty in the unknown parameters for this technique were obtained by Cramer-Rao lower bound analysis [25]. For a measurement that is a function of a set of unknown parameters, $\hat{\alpha}_i$, the variance of the estimates of the parameters is:

$$V(\hat{\alpha}_i) = \left[\Gamma^{-1}\right]_{ii} \tag{13}$$

where the Fisher information matrix for Poisson statistics is given by:

$$\Gamma_{i,j} = \sum_q \frac{1}{\langle N_q \rangle} \frac{\partial \langle N_q \rangle}{\partial \alpha_i} \frac{\partial \langle N_q \rangle}{\partial \alpha_j} \tag{14}$$

Using the model function (12) developed for $\langle N_q \rangle$, the uncertainty or standard deviation $\sigma(\hat{\alpha}_i)$ in each unknown parameter may be determined by calculation and inversion of the Fisher information matrix.

If a Gaussian spectrum is assumed, the lower bounds for uncertainties in the instantaneous temperature T, velocity u_k, and density ρ measurements for an ideal instrument are:

$$\frac{\sigma(T)}{T} = \left(\frac{2}{\langle N_R \rangle}\right)^{1/2}$$
$$\frac{\sigma(u_k)}{a} = \left(\frac{1}{2\langle N_R \rangle}\right)^{1/2} \tag{15}$$
$$\frac{\sigma(\rho)}{\rho} = \left(\frac{1}{\langle N_R \rangle}\right)^{1/2}$$

For air flow at T = 295 K, u_k = 10 m/s, and standard pressure, the lower bound uncertainty estimates for a sampling rate of 32 kHz and typical experiment parameters, assuming an *ideal* instrument, are:

$$\frac{\sigma(T)}{T} = 2.0\% \qquad \sigma(u_k) = 4.2\,\text{m/s} \qquad \frac{\sigma(\rho)}{\rho} = 1.2\%$$

For any *real* instrument, these measurement uncertainties will be higher. The actual Cramer-Rao lower bound measurement uncertainties were calculated, given the FPI, PMTs, and overall efficiency of the current system at sampling rates of 16 and 32 kHz. The TENTI S6 spectral model was used to calculate the Rayleigh scattering spectrum in this analysis rather than using the simpler, less accurate Gaussian model used in the analysis above [20,23]. Fig. 5 shows the

absolute uncertainty in T for a static temperature of 295 K and a range of velocities from -200 m/s to 200 m/s for two sampling rates and probe volume (PV) lengths. As Eq. (15) indicates, the uncertainty is inversely related to the square-root of the number of photoelectron counts. Therefore, the uncertainty increases with increasing sampling rate since the integration time over which photons are collected for each individual sample is shortened. One way to counteract the increase in uncertainty due to increasing the sampling rate is to increase the number of scattered photons in some other way, such as increasing laser power or increasing the PV size. Fig. 5 demonstrates that if the PV length is doubled the uncertainty levels for 32 kHz sampling rate will be equal to the uncertainty of the 16 kHz rate with half the PV length. In the current experiment, the PV was 1.1 mm, which was approximately 1/10 of the jet diameter. In larger facilities an increase in PV size may be a viable solution for reducing uncertainty levels as long as the ratio of PV length to the facility length scale is kept reasonably small.

Fig. 6 illustrates the expected instantaneous temperature uncertainty levels for a mean velocity of 10 m/s and temperatures ranging from 250 to 750 K. The solid circles indicate the portion of the curves that apply to the temperature fluctuation validation study. Fig. 7 gives the absolute uncertainty in u_k over the same range of temperatures and a mean velocity of 10 m/s. The solid circles indicate the points relevant to the velocity fluctuation validation experiment. The measurement uncertainties for T and u_k increase as temperature increases. This is attributable to the lower gas density at higher temperatures, resulting in fewer scattering molecules, and hence fewer scattered photons. Although the uncertainty in the parameters is rather high for instantaneous measurements, long data records allow for calculation of higher accuracy statistical quantities such as power spectra and mean square fluctuations. Experimental data was acquired at sampling rates of 16 and 32 kHz. The photon count values were a factor of 2 greater for the lower sampling rate; therefore the uncertainty levels are a factor of $\sqrt{2}$ better than those at the higher sampling rate.

The Cramer-Rao lower bound analysis was used to optimize the experiment parameters, such as magnification factor, reference fringe radius (r_R), and the radii of the fringe dissection mirrors. The parameters were varied in the model until the uncertainty levels in both T and u_k were minimized [18]. A r_R value of 6.5 mm, image magnification of 35, and dissection mirror radii of 2.5 mm, 6 mm, 8 mm, and 12.5 mm were chosen for the experiments.

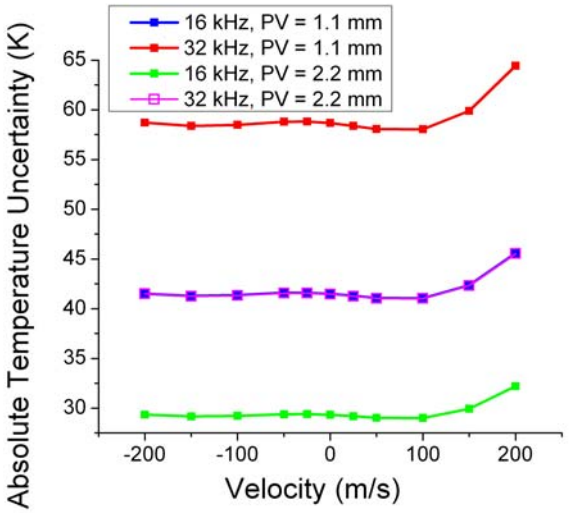

Figure 5. Absolute temperature uncertainty as a function of velocity for two sampling rates and probe volume (PV) lengths.

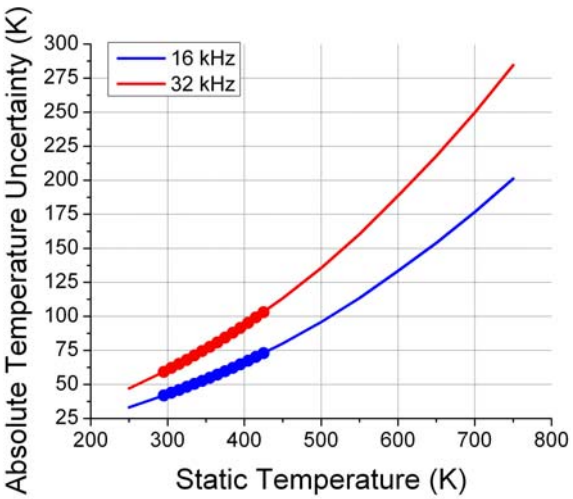

Figure 6. Absolute temperature uncertainty as a function of temperature for the two sampling rates used in these experiments and PV = 1.1 mm.

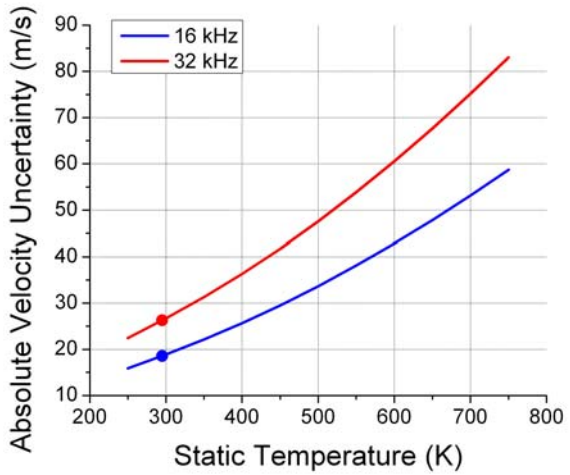

Figure 7. Absolute velocity uncertainty as a function of temperature for the two sampling rates used in these experiments and PV = 1.1 mm.

C. Simulation of 'real' data

The model function given in Eq. (12) was used to generate photon count data based on input velocity and temperature values. A time record of oscillating temperature or velocity similar to the values expected in our experiments was provided as input for the simulation by assuming a sinusoidal flow response to a sinusoidal acoustic excitation. For each sample in the time record ideal (noise-free) data were computed in terms of expected photon counts from each of the 5 PMTs. Poisson noise was added to each photon count value and recorded in a data file. The simulated data record was then read into another program that performed a least-squares fitting routine on the photon counts in the record to determine instantaneous velocity and temperature values, identical to the data analysis performed on *real* data acquired in the experiments. The purpose of the simulation exercise is three-fold:

1. To validate that noise contributions in the experiment are understood
2. To evaluate baseline noise levels in the current experiment
3. To provide a design/optimization tool for future experiments in large test facilities

The simulated data will be presented and discussed in section IV.

III. Experiment

Two jet flow systems were used to evaluate the performance of the Rayleigh scattering flow diagnostic. An acoustically modulated nozzle flow was used to validate velocity fluctuation measurements. The amplitude and frequency of the velocity fluctuations were verified by constant temperature anemometry (CTA) measurements. An asymmetric oscillating counterflow with unequal enthalpies was used to evaluate the ability of Rayleigh scattering to measure temperature fluctuations accurately by comparison with constant current anemometry (CCA) measurements. The details of the two experiments will be discussed in this section.

A. Acoustically modulated nozzle flow

In the first experiment, flow measurements were performed in an air stream issuing from a jet consisting of a converging nozzle with a 10 mm exit diameter (fig. 8). The jet was coupled to a loudspeaker, which provided pressure waves that induced velocity fluctuations of a known driving frequency in the exiting flow. A function generator provided a sine wave input to the amplifier, which allowed variation of the signal amplitude sent to the speaker diaphragm. Since the measurement technique relies on having particulate free gas flow, a series of filters were placed in line with the air plumbing to remove dust, oil and water from the air supply. Fig. 8 shows the layout of the optics around the jet, which were used to collect Rayleigh scattered light from gas molecules in the flow. The jet was mounted such that the main flow direction was parallel to the table. A 10W, 532 nm wavelength, single-frequency, Nd:Vanadate cw laser provided incident light for the system. The laser beam was focused with a 250 mm focal length lens (L1) to a 70 μm $1/e^2$ diameter at the probe volume. The beam was oriented in the horizontal plane, at a 45^o angle to the primary flow direction. Light was collected at a 90^o scattering angle, collimated by a f/4 200 mm focal length lens (L2), and focused by a 100 mm focal length lens (L3) onto a 0.55 mm diameter multimode optical fiber. Since the pair of lenses provided 1:2 imaging, the length of the probe volume was 1.1 mm. The incident and scattering wave vectors were arranged such that the axial component of the jet velocity was measured, as shown by the **K** vector in Fig. 8. The 1.1 mm probe volume was positioned two jet diameters from the nozzle exit on the flow centerline. The probe volume could not be positioned any closer to the nozzle exit in this configuration due to clipping of the laser beam by the jet hardware. The jet was operated at a mean (steady flow) exit velocity of approximately 10 m/s and static temperature of 295 K, giving a Reynolds number (Re) on the order of 10^4. An oscillating (unsteady) flow field was produced by driving the loudspeaker at a frequency of 50 Hz at fixed amplitude.

For calibration purposes, the mean temperature, density, and velocity at the probe location in a steady flow were calculated via isentropic flow and ideal gas equations using total pressure and temperature measurements acquired by pressure probe and type K thermocouple measurements in the jet plenum and static pressure measurements from an ambient pressure probe. The velocity fluctuations were verified using a CTA (hotwire anemometry) system. A TSI probe (model 1210-T1.5) with a single 3.8 μm diameter, 1.25 mm long platinum-coated tungsten resistance wire was used with a TSI IFA-100 thermal anemometry system operated in a constant temperature configuration using an overheat ratio of 1.4. The frequency response of the CTA system was measured to be greater than 100 kHz. The CTA measurements were obtained at the same location and jet conditions as the Rayleigh data, but were acquired on a different day.

B. Asymmetric oscillating counterflow with unequal enthalpies

In the second experiment, measurements were performed in the flow between opposed heated and unheated air jets issuing from nozzles with 10 mm exit diameters (fig. 9). The unheated jet hardware was identical to that described in the previous section. The filtered air issuing from the opposing jet was heated by applying voltage to coils of kanthal wires inside the jet plenum. The output temperature remained sufficiently steady by applying a constant voltage to the wires while maintaining a fixed air mass flow rate. The temperature of the heated jet was set by monitoring a fine-wire (0.25 mm diameter) open-bead type K thermocouple placed at the jet exit. The loudspeaker was used in this experiment to generate an oscillating flow providing large temperature fluctuations at the probe volume location. Fig. 9(a) shows the layout of the optics around the opposed jet system. The jets were mounted such that the main flow direction was parallel to the table and the nozzle exits were separated by two jet diameters. The 10W, 532 nm wavelength laser beam was focused with a 250 mm

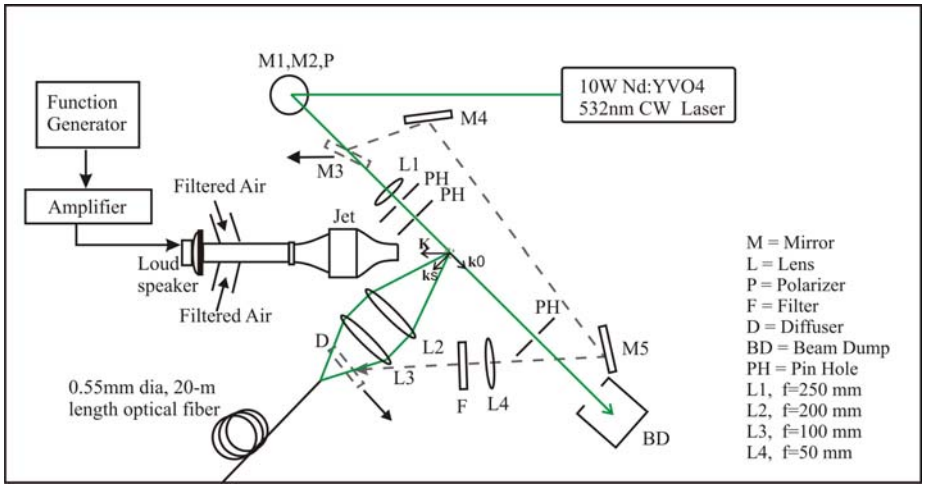

Figure 8. Diagram of laser and collection optics for acoustically-excited nozzle flow experiment

focal length lens (L1) to a 70 μm $1/e^2$ diameter at the probe volume. The beam was oriented in the vertical direction, orthogonal to the primary flow direction. Light was collected at a 90° scattering angle using identical collection optics as described in the previous section, which provided a 1.1 mm probe volume. The incident and scattering wave vectors were arranged such that the radial component of the jet velocity was measured, as shown by the **K** vector in Fig. 9(b). This arrangement was chosen so that velocity fluctuations were minimized since the radial component of the centerline velocity is approximately 0 m/s. The unheated air jet was operated at a mean axial velocity of approximately 10 m/s and static temperature of 295 K (Re ~ 10^4). The heated air jet was operated at a static temperature of 425 K and the momentum (ρu_k^2) was set such that it was matched to the momentum of the unheated jet (Re ~ 10^3). Matching the momentum centered the stagnation plane half-way between the two jets. A shadowgraph system was used to monitor the location of the maximum temperature gradient in the flow. Fig. 10 shows a photograph of the shadowgraph image plane. The imaging screen contains 1 mm x 1 mm squares. Outlines of the nozzle locations are indicated on the left and right sides of the 18 mm diameter laser spot. The region of reduced light intensity (outlined in white) that is centered approximately 9 mm from the hot jet exit is due to deflection of the collimated light rays resulting from the large temperature gradient in the flow. For this experiment, the location of the maximum temperature gradient was positioned approximately half-way between the two nozzles by adjusting the heated jet flow rate. The Rayleigh probe volume was positioned 7 mm from the hot jet exit on the flow centerline where the temperature fluctuations were maximized for an excitation frequency of 100 Hz, as determined by CCA temperature probe measurements.

For system calibration purposes, steady flow static temperature and pressure measurements at the probe location were measured by a fine-wire type K thermocouple and an ambient pressure gauge. Gas density information was derived from these measurements using the ideal gas law. For calibration, the mean radial velocity component was assumed to be 0 m/s. A CCA (coldwire thermometry) system provided static temperature fluctuation measurements in unsteady flows to validate the dynamic Rayleigh technique. A TSI probe (model 1276-P.5) with a 1.3 μm diameter, 0.9 mm long

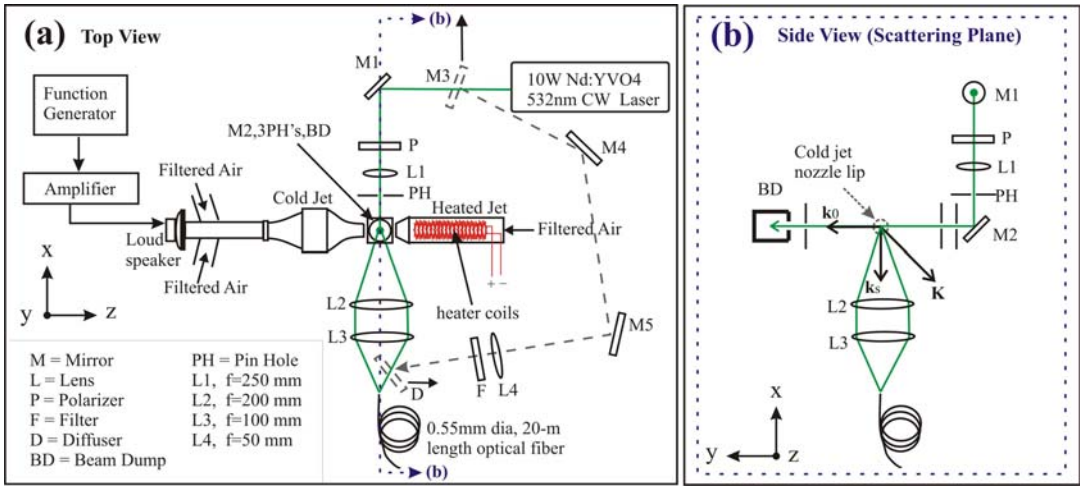

Figure 9. Diagram of laser and collection optics for asymmetric oscillating counterflow experiment.

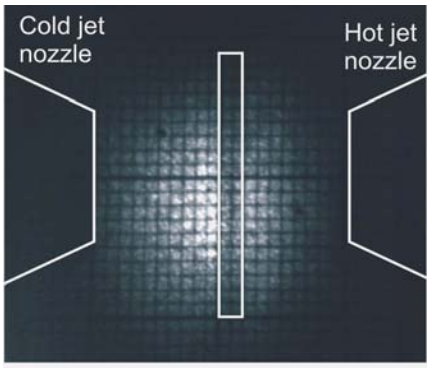

Figure 10. Photograph of the shadowgraph image plane.

platinum resistance wire was used with a TSI 1745 constant current anemometer. The frequency response of the CCA system, based on the 3 dB point, was measured to be just under 1 kHz. CCA measurements were obtained at the same jet conditions as the Rayleigh data; however they were not obtained simultaneously.

C. Spectral analysis and detection optics

The spectral analysis and detection optics were identical for both experiments. Upon collection of the Rayleigh scattered light by the 0.55 mm diameter multimode fiber, it was routed to a separate optical table, shown schematically in Fig. 11. The light exiting the fiber was collimated by an 80 mm focal length lens (L5) and was directed through the planar mirror Fabry-Perot interferometer. The FPI had 70 mm diameter mirrors with 80% reflectivity, 8.7 GHz free spectral range (FSR), and reflective finesse of approximately 15. The Fabry-Perot is an extremely sensitive instrument; even the smallest vibrations or temperature changes can cause the mirrors to drift out of parallel alignment, resulting in increased uncertainty. Therefore, a stabilization system was utilized to maintain parallelism of the mirrors during testing. Between Rayleigh scattering measurements, a mirror and diffuser (shown in dashed gray lines in Figs. 8 and 9) were placed in the beam path by linear actuators to direct some of the incident laser beam into the optical fiber and through the FPI. A set of reflecting prisms mounted on a linear actuator (Fig. 11) were positioned in the optical path at the output of the interferometer to direct the light from three regions of the interferometer mirrors to a video camera. Live video of the three fringe images was used in a feedback control loop to adjust the mirror positions using piezoelectric transducers until the three fringes were equal in diameter. This system was also used to set the fringe diameter of the incident reference light to 13 mm, as determined from the uncertainty analysis. Further details regarding the mirror stabilization system for the FPI can be found in [17].

When flow measurements were acquired, the prisms, mirror, and diffuser were removed from the optical path and the light exiting the FPI was focused by a fringe forming lens (L6) having an effective focal length of 2704 mm, which provided an 18.6 mm diameter image of the fiber face. Light from circular and annular sections of the image were directed toward PMTs by a concentric elliptical mirror system, which was designed and fabricated specifically for this application. A photograph of the 'image dissector' is shown in the upper left corner of Fig. 11. The mirrors were machined from 6061 aluminum and the 12^{o} elliptical surfaces were diamond polished to a mirror finish with about 90% reflectivity. The mirror diameters, from innermost to outermost, are 5 mm, 12 mm, 16 mm, and 25 mm. Each mirror sends the respective portion of the fringe image toward PMTs 1, 2, 3, and 4. Fig. 12 illustrates the individual areas of the fringe image which are directed towards each PMT. A 19.2 mm diameter aperture was centered at the image plane to eliminate stray light and ghost images outside of the fiber image region from being directed by the outermost mirror onto the detector of PMT 4.

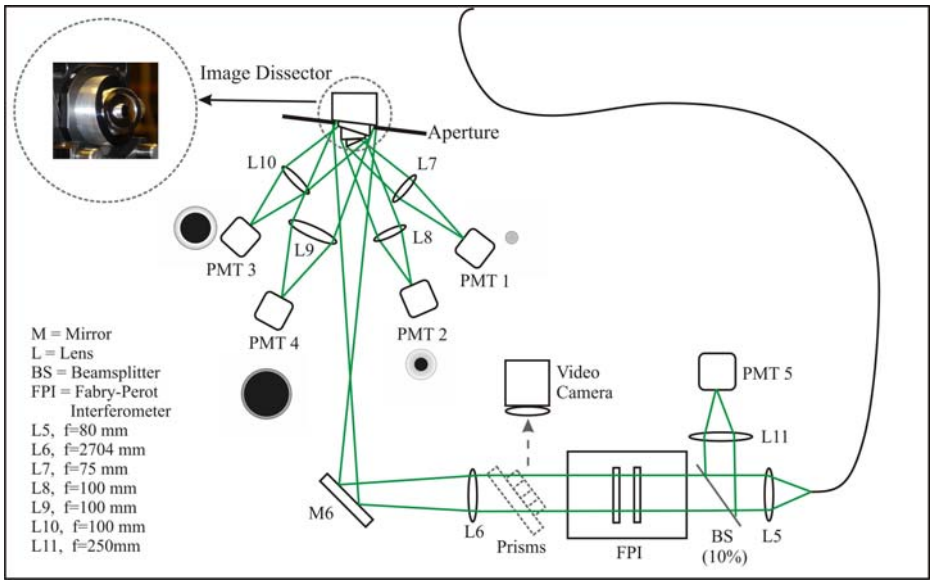

Figure 11. Schematic of spectral analysis and detection optics.

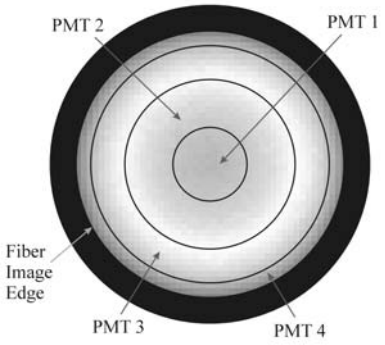

Figure 12. Dissection of Fabry-Perot fringe pattern into one circular and three annular regions.

The PMTs were operated in the photon counting mode to acquire fringe intensity data. The photoelectron pulses from the five PMTs were amplified (Gain = 5) and sent to photon counters, which output NIM level pulses. Constant fraction discriminators converted the NIM pulses to 10 ns wide TTL level pulses that were counted via counter-timer boards. Typical photoelectron count rates for this work were on the order of 1 MHz. A PC-based data acquisition system was used to record the signals from the PMTs. Each signal channel was digitized at either 16 or 32 kHz sampling rate for 10 seconds, resulting in 160,000 or 320,000 samples per channel. The intensity information from the Fabry-Perot fringe sampling was used to obtain temperature and velocity measurements. The density measurement was much simpler, requiring only an overall intensity measurement. A beamsplitter located just in front of the FPI input (Fig. 11) directed approximately 10% of the incoming Rayleigh scattered light to a lens (L11), which focused the light at PMT 5 for the density measurement.

IV. Results

A. *Experiment calibration and data analysis method*

The technique was calibrated over a range of operating points in each flow system. The unheated nozzle flow in the first experiment was operated over a static temperature range of 289 – 295 K and velocity range of 10 – 150 m/s. The heated jet in the second experiment was operated over a static temperature range of 295 – 550 K with mean radial velocity component assumed as 0 m/s. The unheated jet was not running for the calibration portion of this experiment. The photoelectron counts recorded by PMT 5 are linearly related to density, providing an independent yet simultaneous measurement of density along with the velocity and temperature measurements from spectroscopic analysis. The axial or radial velocity component and temperature were measured by analyzing the light from the circular and annular regions of the interference fringe pattern at the output of the FPI. The model of the fringe pattern (Eq. (12)), was used in a least-squares fitting routine to estimate unknown parameters from the intensity data. For calibration, mean temperature, velocity, and pressure measured by physical probes or calculated from the isentropic flow and ideal gas relations were used as known values in the model function. Several unknown factors were evaluated by least-squares analysis of the mean photon count data at the calibration points. These unknown factors included system detection efficiencies, effective finesse of the FPI, and fringe forming lens focal length. Once determined, these factors were input in the model function for use in least-squares analysis of the PMT counts for temperature and velocity measurements.

Using the linear relation between PMT 5 photon counts and density, and least-squares analysis of the photon counts from PMTs 1-4, time histories of instantaneous density, temperature, and velocity were evaluated. The density measured by PMT 5 was used in the fitting of the spectral data to provide pressure information via the ideal gas law, making this measurement technique applicable in flows where the pressure is unknown and the ideal gas law is valid.

The mean velocity and temperature were calculated and subtracted from their respective time history records to provide zero-mean records, which were used to calculate the power spectral densities of the property fluctuations. Because of the shot noise in the PMT signals, it was necessary to use relatively long data records and calculate power spectra using a technique such as the Welch method of modified periodograms [26]. Due to extensive processing time of the Rayleigh data (approximately 1000 samples/min), only the first 2.56 seconds of the data were analyzed. In the Welch method, a data record sampled at a rate f_s = 16 kHz (32 kHz) was subdivided into 38 smaller records of length L = 2048 (4096) samples, which were overlapped by 50%. The modified periodograms of each sub-record were calculated using a data window. These individual periodograms were then averaged to obtain the estimate of the power spectrum. The frequency resolution of the resulting spectra is f_s / L = 7.8125 Hz. The coldwire data was sampled at only 1 kHz due to the response limit of the system. Sampling rates were chosen so that the power spectra for all rates resulted in the same frequency resolution, and the power levels in each frequency bin could be directly compared. Overlapping the segments by 50% provided a near maximum reduction in the variance in the spectral estimate. The resulting power spectra provide fluctuation information out to 8 kHz (16 kHz), and the sum of all points in the spectra is equivalent to the mean square fluctuations.

B. *Simulation and experimental data from the acoustically modulated jet experiment*

The unheated nozzle flow was operated at a mean velocity of 10 m/s while the flow velocity was perturbed by acoustically-induced pressure waves emanating from a loudspeaker which was driven by a sinusoidal voltage input with a frequency of 50 Hz. Other excitation frequencies and fluctuation amplitudes were investigated; however in the interest of space only this representative case is presented in this paper. Flow measurements were made using the Rayleigh technique and hotwire anemometry (CTA). The hotwire instrumentation was sampled at 16 kHz; however Rayleigh measurements were acquired at 16 and 32 kHz sampling rates. While all three flow

parameters (ρ, T, u_k) were measured using the Rayleigh technique, only velocity results are presented here since the temperature and density fluctuations were expected to be very small. Simulated velocity data was generated assuming a purely sinusoidal flow response at the fundamental frequency of 50 Hz. A short segment of the time-history and the power spectrum calculated from the full time-history record of the simulated velocity measurements for a sampling rate of 16 kHz are shown in figs. 13 and 14, respectively. The input (ideal) velocity function is shown for comparison. The time-histories and power spectra of experimental data (Rayleigh and hotwire measurements) acquired at 16 kHz sampling rate in a similar flow scenario as that of the simulation are presented in figs. 15 and 16, respectively. Power spectral information is available up to half of the sampling frequency, however only the first 1000 Hz of the spectra are shown because the spectra are very flat beyond that point due to lack of significant fluctuations at high frequencies. Simulated and experimental flow data for the same flow conditions are shown for a sampling rate of 32 kHz in figs. 17-20. The experimental power spectra for both the Rayleigh and hotwire data indicate that fluctuations are present at the fundamental driving frequency as well as harmonics of that frequency. The source of these harmonic fluctuations was investigated by measuring the displacement of the speaker diaphragm during operation using an Ometron VPI sensor (model 8330) scanning laser doppler vibrometer. Fig. 21 shows the power spectrum of speaker displacements determined by the vibrometer measurements, which verifies the presence of harmonic frequency components in the speaker output. The presence of these harmonic disturbances leads to the asymmetric nature of the periodic velocity fluctuations. Figs. 22 and 23 show time-history and power spectra of simulated data having an input function that is a summation of sinusoidal components at the fundamental and nine harmonic frequencies as given by the following equation, where $N = 10$ and $A(i)$ is the signal amplitude at the i^{th} multiple of the fundamental frequency (f_{fund}):

$$signal = \sum_{i=1}^{N} \left[A(i) \sin\left(2\pi (f_{fund} \cdot i) t\right) \right] + mean \qquad (16)$$

The simulated flow response function has an asymmetric nature similar to that of the experimental data. This is a very simplistic model of flow response to a multiple-frequency sinusoidal disturbance. Many other factors have been ignored in the model, such as viscous effects; however the purpose of this exercise is not to model the flow phenomena, but rather to demonstrate that the Rayleigh experiment simulation can accurately model the light scattering and detection processes.

The time-history plots of the experimental and simulated Rayleigh data show that random noise levels are comparable. This is further verified by the baseline noise levels calculated from the power spectra. In each figure showing power spectral data (figs. 14, 16, 18, 20, and 23) a baseline noise level has been indicated, which was found by averaging the power levels over the last 1000 Hz (128 points) of the spectrum where insignificant flow fluctuations exist and the spectrum has leveled out. Based on a frequency bin width of 7.8125 Hz, the baseline power level was used to calculate the lower bound of the velocity fluctuation level that can be measured via these second-order statistical calculations. Recall from the earlier uncertainty analysis that the lower bound on the instantaneous velocity measurements was on the order of 18-27 m/s. The lower-bound uncertainty in velocity fluctuation amplitude calculated from second-order statistics is on the order of 2 m/s. Notice that the lower-bound values determined from the simulated data are nearly equivalent to the values determined from the experimental data statistical calculations. The baseline noise level is mostly due to Poisson noise inherent in the photon detection process. Poisson noise is random and therefore contributes equally over all frequencies; hence the baseline noise level can be subtracted from all points in the power spectrum to provide a more accurate spectral estimation. This is a unique feature of the power spectrum that allows random noise contribution to be 'filtered' from second-order statistical quantities, such as mean square fluctuations.

An additional observation to note about the experimental power spectra is the good comparison between the spectra acquired from Rayleigh and hotwire measurements up until the point where the velocity fluctuation levels fall below the lower-bound of the Rayleigh measurement capability. Slight amplitude differences exist due to the noise pedestal of the Rayleigh power spectra, as well as minor dissimilarities in the flow at the time of the two non-simultaneous measurements. Keep in mind that the hotwire is a physical probe that intrusively provides the velocity measurement. The probe itself may be causing some of the dissimilarities mentioned. One major difference between the Rayleigh and hotwire measurements is a band of large velocity fluctuations in the 640 – 700 Hz frequency range that are observed in the Rayleigh power spectra but are not present in the hotwire spectra. These velocity fluctuations are not actually present in the flow. The laser used in these experiments has a tendency to exhibit resonance in its output at various frequencies. These resonances are often amplified when external noise sources, like the loudspeaker, are present. A peak in this same frequency range was observed in other velocity measurements acquired using this same laser, even in flows where no acoustic modulation was present. Modulation of the laser frequency shows up as apparent velocity fluctuations since velocity is determined by measuring a shift in the light frequency.

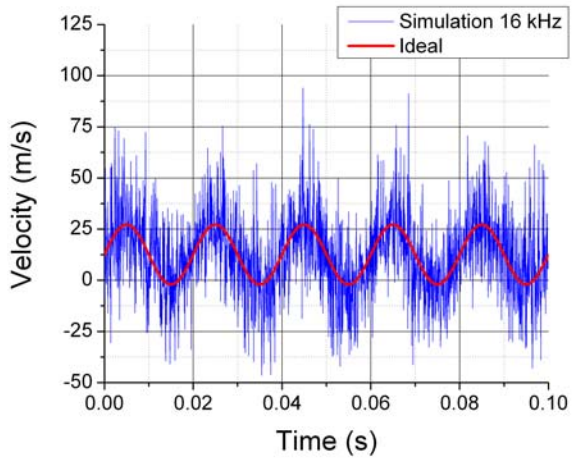

Figure 13. Simulated velocity data for 50 Hz sinusoidal velocity perturbation with mean = 12.6 m/s and amplitude = 14.6 m/s, sampled at 16 kHz.

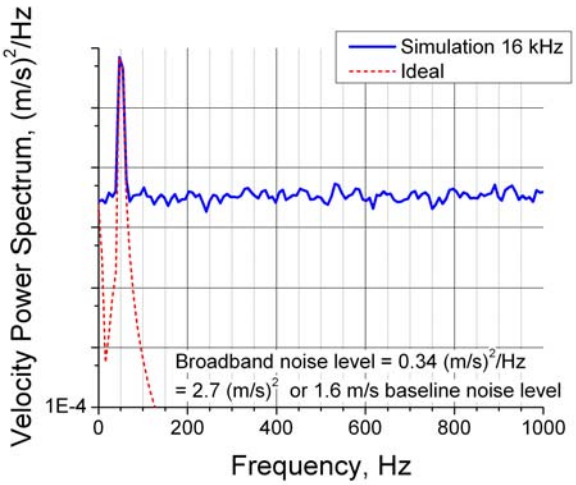

Figure 14. Power spectra of simulated velocity data from fig. 13.

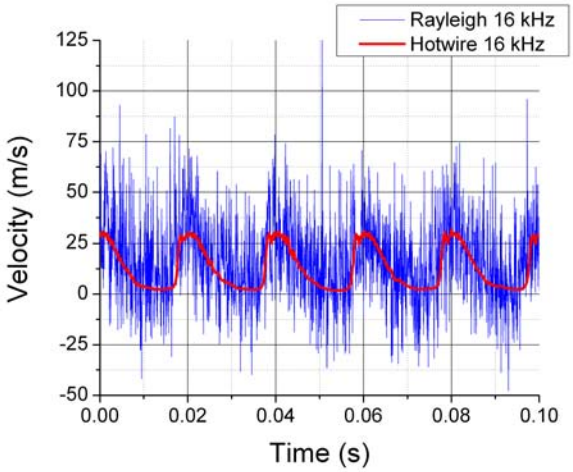

Figure 15. Experimental velocity data for a sinusoidal velocity perturbation with fundamental frequency of 50 Hz, sampled at 16 kHz.

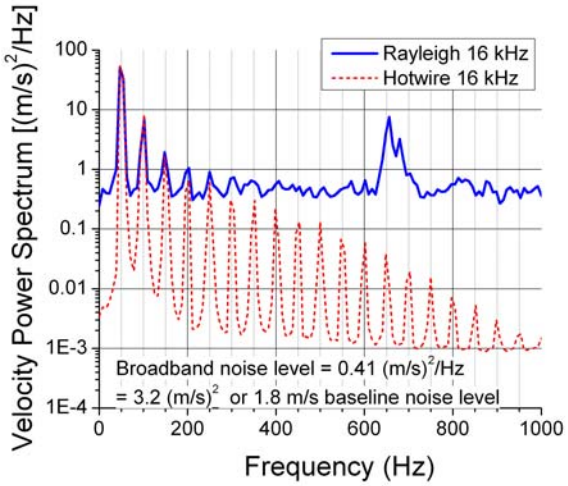

Figure 16. Power spectra of experimental velocity data from fig. 15.

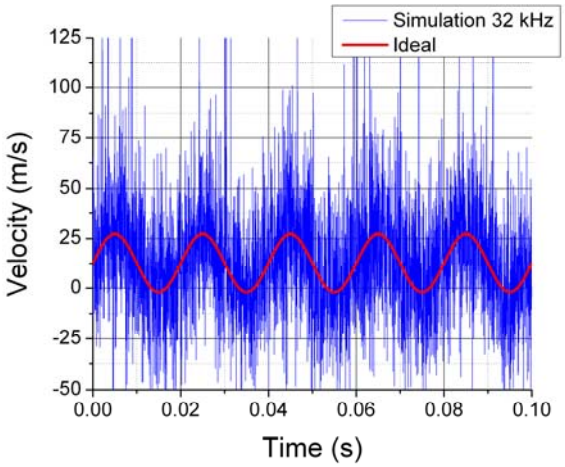

Figure 17. Simulated velocity data for 50 Hz sinusoidal velocity perturbation with mean = 12.6 m/s and amplitude = 14.6 m/s, sampled at 32 kHz.

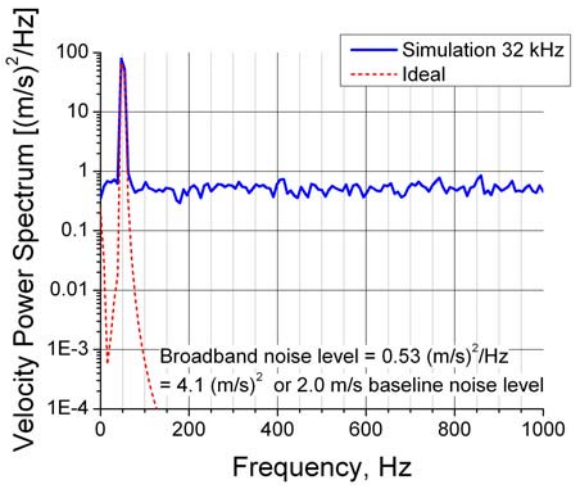

Figure 18. Power spectra of simulated velocity data from fig. 17.

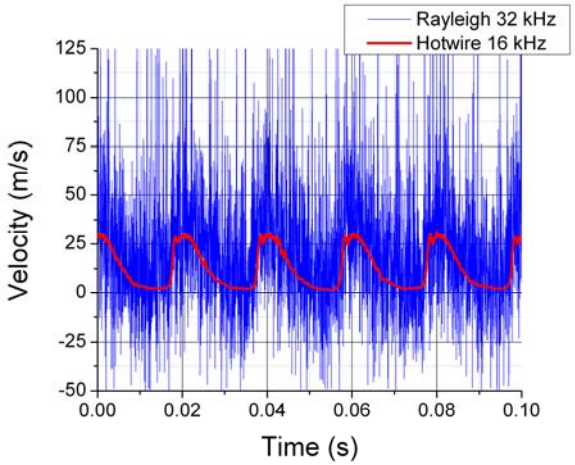

Figure 19. Experimental velocity data for a sinusoidal velocity perturbation with fundamental frequency of 50 Hz. Rayleigh data sampled at 32 kHz and hotwire data sampled at 16 kHz.

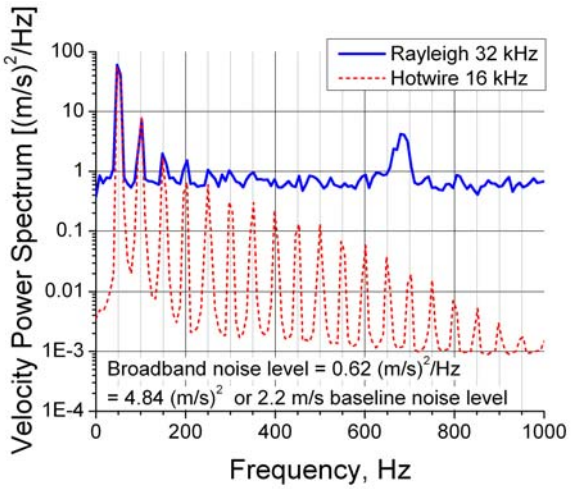

Figure 20. Power spectra of experimental velocity data from fig. 19.

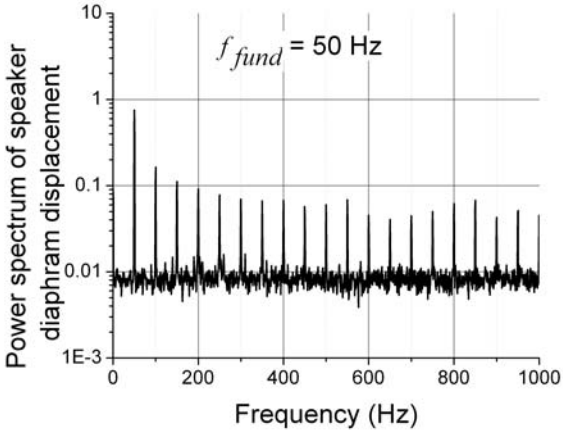

Figure 21. Power spectrum of speaker diaphragm displacement measured by a scanning laser doppler vibrometer showing harmonic components in the speaker output.

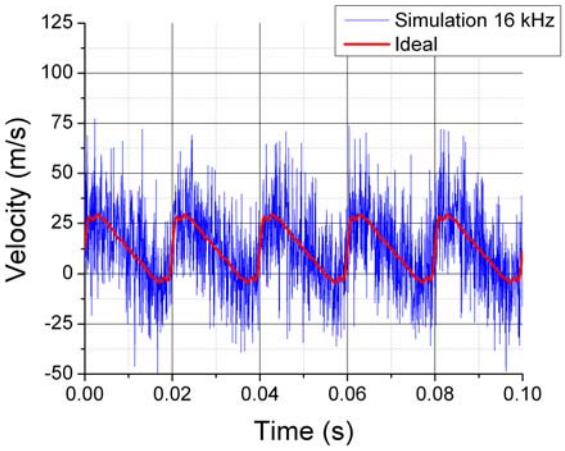

Figure 22. Simulated 16 kHz rate velocity data for 50 Hz fundamental sinusoidal velocity perturbation with mean = 12.6 m/s and A(i) = 14.6, 5.7, 2.6, 1.6, 1.5, 1.1, 1.08, 0.94, 0.72, 0.7 m/s for i = 1 to 10, where A(1) is the amplitude at the fundamental frequency and A(i) is the amplitude at the i^{th} harmonic frequency.

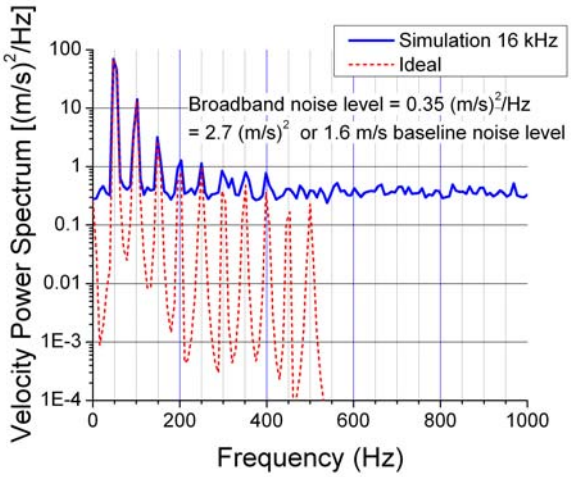

Figure 23. Power spectra of simulated velocity data from fig. 22.

C. Simulated and experimental data from the asymmetric oscillating counterflow with unequal enthalpies experiment

A counterflow with unequal enthalpies was perturbed by acoustically-induced pressure waves emanating from a loudspeaker in the unheated jet plumbing which was driven by a sinusoidal voltage input with a frequency of 100 Hz. Other excitation frequencies and fluctuation amplitudes were investigated; however only this representative case is presented here. Flow measurements were made using the Rayleigh technique and coldwire thermometry (CCA). The Rayleigh measurements were acquired at 16 and 32 kHz sampling rates, whereas the coldwire instrumentation was limited to a sampling rate of 1 kHz. All three flow parameters (ρ, T, u_k) were measured using the Rayleigh technique, however only temperature results are presented here since the velocity fluctuations were expected to be very small and the density measurement is trivial and has been demonstrated in previous work [17,28]. Simulated temperature data was generated assuming a flow response consisting of a summation of

sinusoidal functions at the fundamental frequency of 100 Hz and three additional harmonic frequencies using Eq. (16). A short segment of the time-history and the power spectrum calculated from the full time-history record of the simulated temperature measurements assuming a sampling rate of 16 kHz are shown in figs. 24 and 25, respectively. The input (ideal) temperature function is shown for comparison. The time-histories and power spectra of experimental temperature data (Rayleigh and coldwire measurements) acquired at 16 kHz sampling rate in a similar flow scenario as that of the simulation are presented in figs. 26 and 27. Simulated and experimental flow data for the same flow conditions are shown for a sampling rate of 32 kHz in figs. 28-31. Again, only the first 1000 Hz of the much longer power spectra are shown, and the experimental power spectra for both the Rayleigh and hotwire data indicate the presence of harmonic frequency components due to harmonic distortion in the loudspeaker output.

The time-history plots of simulated and experimental temperature data show comparable levels of random noise. The noise levels at the maximum flow temperature are greater than the noise levels at the minimum temperature as a result of a lower molecular number density at the higher temperature. The baseline random noise levels calculated from the power spectra (indicated in figs. 25, 27, 29, and 31) are nearly equal for the simulated and experimental cases. Recall from the earlier uncertainty analysis that the lower bound on instantaneous temperature measurements was predicted to be on the order of 40 – 100 K. The lower-bound uncertainty in the temperature fluctuation amplitude calculated from second-order statistics in on the order of 7 – 9 K.

The experimental power spectra exhibit some significant amplitude differences between the Rayleigh and coldwire measurements at the harmonic frequencies; although the amplitudes at the fundamental frequency compare pretty well. Even with subtraction of the random noise pedestal, the amplitude levels at the harmonic frequencies are still an order of magnitude different. One possible explanation is that the physical coldwire probe has a significant influence on the fluctuating flow field that causes an amplitude reduction in the temperature fluctuations. The position of the coldwire probe in the flow was observed to have an effect on the location of the maximum temperature gradient via the shadowgraph instrumentation. This observation leads us to believe that the coldwire probe may not provide an accurate measurement of the oscillating temperature field. The limited frequency response of the coldwire probe may also be a contributing factor. This situation reiterates the need for a non-intrusive measurement technique.

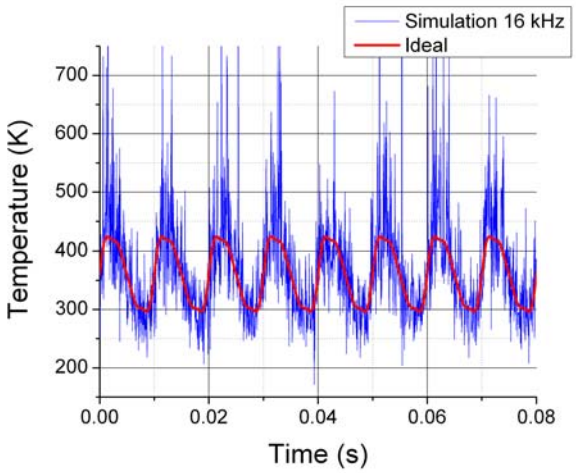

Figure 24. Simulated 16 kHz rate temperature data for 100 Hz fundamental sinusoidal velocity perturbation with mean = 360 K and A(i) = 65.9, 10.6, 8.4, 4.4 K for i = 1 to 4, where A(1) is the amplitude at the fundamental frequency and A(i) is the amplitude at the i^{th} harmonic frequency.

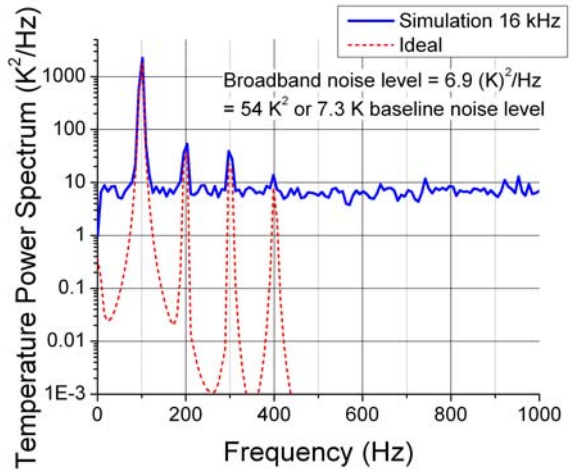

Figure 25. Power spectra of simulated temperature data from fig. 24.

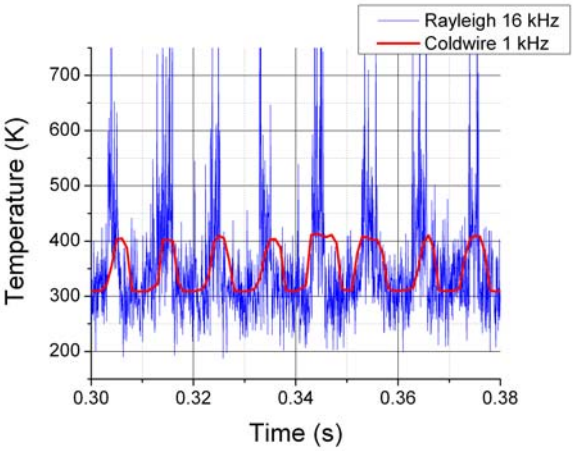

Figure 26. Experimental temperature data for a sinusoidal temperature perturbation with fundamental frequency of 100 Hz. Rayleigh data is sampled at 16 kHz and coldwire data is sampled at 1 kHz.

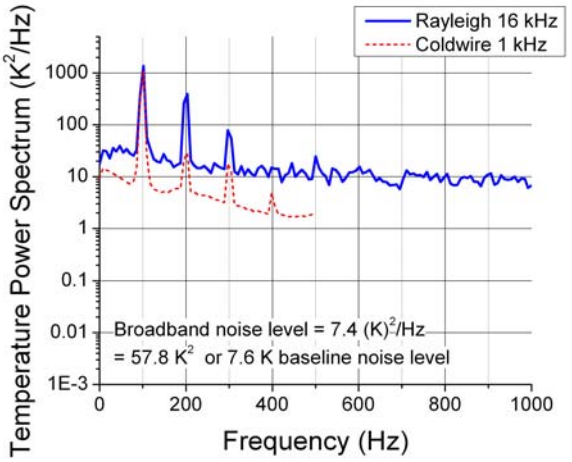

Figure 27. Power spectra of experimental temperature data from fig. 26.

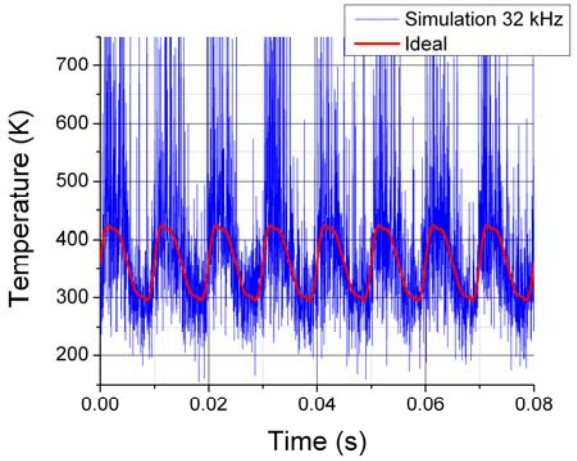

Figure 28. Simulated 32 kHz rate temperature data for 100 Hz fundamental sinusoidal velocity perturbation with mean and A(i) values same as in fig. 24.

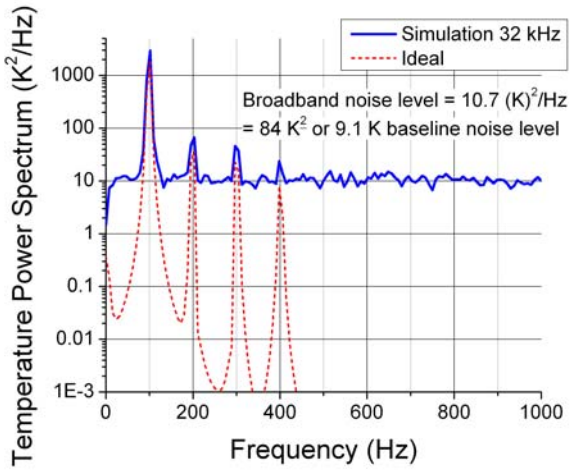

Figure 29. Power spectra of simulated temperature data from fig. 28.

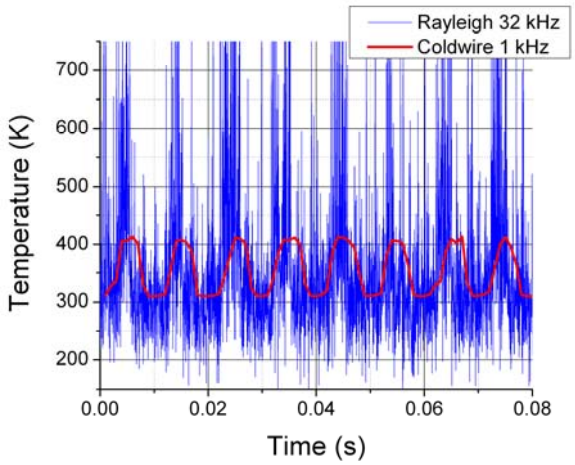

Figure30. Experimental temperature data for a sinusoidal temperature perturbation with fundamental frequency of 100 Hz. Rayleigh data is sampled at 32 kHz and coldwire data is sampled at 1 kHz.

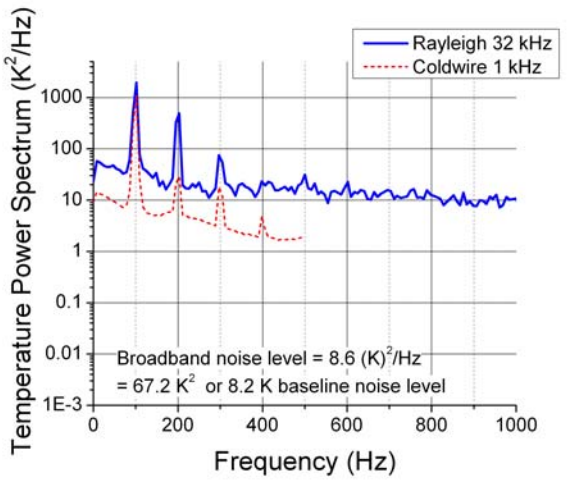

Figure 31. Power spectra of experimental temperature data from fig. 30.

V. Conclusions and Future Work

A technique for obtaining time-resolved gas velocity, temperature, and density measurements using molecular Rayleigh scattering was described. Density was determined from an overall intensity measurement of the scattered light, while temperature and velocity were determined by analyzing the scattered light with a Fabry-Perot interferometer. The signals from five photomultiplier tubes were simultaneously recorded using photon counting at sampling rates up to 32 kHz. An uncertainty analysis was presented that demonstrated uncertainties in instantaneous temperature and velocity measurements of about 20% and 27 m/s, respectively, for a 32 kHz sampling rate. Other statistical quantities, such as mean square fluctuations and power spectra, can be obtained with higher accuracy. The Rayleigh technique was demonstrated in two experiments involving acoustic modulation of the flow field. An acoustically modulated unheated nozzle flow was used to validate velocity fluctuation measurements by comparison with hotwire measurements. An asymmetric oscillating counterflow with unequal enthalpies was studied to

validate temperature fluctuations by comparison with coldwire measurements. A numerical simulation of the spectral analysis and detection process was developed that included relevant noise sources, including Poisson noise. The simulation provides a useful tool for designing future experiments in large test facilities where run-time is limited and expensive. The simulation was validated by comparison with experimental data.

The presented Rayleigh scattering technique will be applied toward aeronautics research at NASA GRC. In addition to the upcoming tests in the SHJAR facility, future work also includes the integration of a Rayleigh scattering system in the 15 x 15 cm supersonic wind tunnel at GRC, which is capable of generating flows up to Mach 3.5, to provide time-resolved flow measurements in the presence of shocks. A multiple-point measurement system is planned for development in this facility to provide mass flux measurement capabilities. This work is in support of NASA's Supersonics and Hypersonics programs.

ACKNOWLEDGMENT

We would like to thank Dick Seasholtz and Mark Wernet for their technical advice.

REFERENCES

[1] A. Eckbreth, *Laser Diagnostics for Combustion Temperature and Species*. Amsterdam: Gordon and Breach Science Publishers SA, pp.209-451, 1996.

[2] E. Cummings, "Laser-Induced Thermal Acoustics," Ph.D. Dissertation, Department of Engineering and Applied Science, California Institute of Technology, Pasadena, CA, 1995.

[3] R. Hart, R. Balla, and G. Herring, "Nonresonant Referenced Laser-Induced Acoustics Thermometry in Air," *Appl Optics*, vol. 38, pp. 577-584, 1999.

[4] Y. Li, W. Roberts, and M. Brown, "Investigation of Gaseous Acoustic Damping Rates by Transient Grating Spectroscopy," *AIAA Journal*, vol. 40, pp. 1071-1077, 2002.

[5] J. Lau, P. Morris, and M. Fisher, "Measurements in Subsonic and Supersonic Free Jets Using a Laser Velocimeter," *J Fluid Mech*, vol. 93, pp. 1-27, July 1979.

[6] J. Lau, M. Whiffen, M. Fisher, and D. Smith, "A Note on Turbulence Measurements with a Laser Velocimeter," *J Fluid Mech*, vol. 102, pp. 353-366, Jan 1981.

[7] R. Flack, "Influence of Turbulence Scale and Structure on Individual Realization Laser Velocimeter Biases," *J Phys E: Sci Instrum*, vol. 15, pp. 1038-1044, 1982.

[8] D. Heist, and I. Castro, "Point Measurement of Turbulence Quantities in Separated Flows - A Comparison of Techniques," *Meas Sci Technol*, vol. 7, pp. 1444-1450, 1996.

[9] R. Huffman, G. Elliott, and M. Boguszko, "Turbulence measurements using FARRS in a Supersonic Axisymmetric Jet," AIAA-2007-471, January 2007.

[10] M. Wernet, "Temporally Resolved PIV for Space-Time Correlations in Both Cold and Hot Jet Flows," *Meas Sci Technol*, vol. 18, pp. 1387-1403, 2007.

[11] S. Garg, and G. Settles, "Measurements of a Supersonic Turbulent Boundary Layer by Focusing Schlieren Deflectometry," *Exp Fluids*, vol. 25, pp. 254-264, 1998.

[12] R. Seasholtz, and L. Greer, "Rayleigh Scattering Diagnostic for Measurement of Temperature and Velocity in Harsh Environments," AIAA-98-0206, January 1998.

[13] J. Panda, and R. Seasholtz, "Velocity and Temperature Measurement in Supersonic Free Jets Using Spectrally Resolved Rayleigh Scattering," AIAA-99-0296, January 1999.

[14] A. Mielke, R. Seasholtz, K. Elam, and J. Panda, "Time-Average Measurement of Velocity, Density, Temperature, and Turbulence Velocity Fluctuations Using Rayleigh and Mie Scattering," *Exp Fluids*, vol. 39, 441-454, 2005.

[15] J. Lock, R. Seasholtz, and W. John, "Rayleigh-Brillouin Scattering to Determine One-Dimensional Temperature and Number Density Profiles of a Gas Flow Field," *Appl Optics*, vol. 31, pp. 2839-2848, 1992.

[16] R. Seasholtz, and J. Panda, "Rayleigh Scattering Diagnostic for Dynamic Measurement of Velocity and Temperature," AIAA-99-0641, January 1999.

[17] R. Seasholtz, J. Panda, and K. Elam, "Rayleigh Scattering Diagnostic for Measurement of Velocity and Density Fluctuation Spectra," AIAA-2002-0827, January 2002.

[18] A. Mielke, K. Elam, and C. Sung, "Rayleigh Scattering Diagnostic for Measurement of Temperature, Velocity, and Density Fluctuation Spectra," AIAA-2006-837, January 2006.

[19] A. Mielke, K. Elam, and C. Sung, "Molecular Rayleigh Scattering Diagnostic for Dynamic Temperature, Velocity, and Density Measurements," AIAA-2006-2969, June 2006.

[20] G. Tenti, C. Boley, and R. Desai, "On the Kinetic Model Description of Rayleigh-Brillouin scattering from Molecular Gases," *Can J Phys*, vol. 52, pp. 285-290, 1974.

[21] R. Sandoval, and R. Armstrong, "Rayleigh-Brillouin Spectra in Molecular Nitrogen," *Phys Rev A*, vol. 13, pp. 752-757, 1976.

[22] S. Yip, and M. Nelkin, "Application of a Kinetic Model to Time-Dependent Density Correlations in Fluids," *Phys Rev*, vol. 135, pp. A1241-A1247, 1964.

[23] C. Boley, R. Desai, and G. Tenti, "Kinetic Models and Brillouin Scattering in a Molecular Gas," *Can J Phys*, vol. 50, pp. 2158-2173, 1972.

[24] J. Vaughan, *The Fabry Perot Interferometer, History, Theory, Practice, and Applications*. Philadelphia: Adam Hilger, 1989, pp. 89-134.

[25] A. Whalen, *Detection of Signals in Noise*. New York: Academic Press, pp. 327-332, 1971.

[26] P. Welch, "The Use of Fast Fourier Transform for the Estimation of Power Spectra: A Method Based on Time Averaging Over Short, Modified Periodograms," *IEEE Trans on Audio and Electroacoustics*, vol. AU-15, pp. 70-73, 1967.

[27] A. Oppenheim, and R. Schafer, *Digital Signal Processing*. New Jersey: Prentice-Hall, pp. 554-555, 1975.

[28] J. Panda, R. Seasholtz, K. Elam, A. Mielke, D. Eck, "Effect of heating on turbulent density fluctuations and noise generation from high speed jets," AIAA-2004-3016, May 2004.